

Complex Time Evolution in Tensor Networks

M. Grundner ^{1,2,*} P. Westhoff ^{1,2} F. B. Kugler ³ O. Parcollet ^{3,4} and U. Schollwöck ^{1,2}

¹*Department of Physics and Arnold Sommerfeld Center for Theoretical Physics (ASC), Ludwig-Maximilians-Universität München, D-80333 Munich, Germany*

²*Munich Center for Quantum Science and Technology (MCQST), D-80799 München, Germany*

³*Center for Computational Quantum Physics, Flatiron Institute, 162 5th Avenue, New York, NY 10010, USA*

⁴*Université Paris-Saclay, CNRS, CEA, Institut de Physique Théorique, 91191, Gif-sur-Yvette, France*

(Dated: December 20, 2023)

Real-time calculations in tensor networks are strongly limited in time by entanglement growth, restricting the achievable frequency resolution of Green's functions, spectral functions, self-energies, and other related quantities. By extending the time evolution to contours in the complex plane, entanglement growth is curtailed, enabling numerically efficient high-precision calculations of time-dependent correlators and Green's functions with detailed frequency resolution. Various approaches to time evolution in the complex plane and the required post-processing for extracting the pure real-time and frequency information are compared. We benchmark our results on the examples of the single-impurity Anderson model using matrix-product states and of the three-band Hubbard-Kanamori and Dworin-Narath models using a tree tensor network. Our findings indicate that the proposed methods are also applicable to challenging realistic calculations of materials.

I. INTRODUCTION

[24–29]

The time evolution of quantum many-body systems such as solids or ultracold gases out of equilibrium is of central interest in physics. Experimental results both in the linear response regime and far from equilibrium may be resolved in real time, such as in pump-probe experiments on solids or in quantum simulations in ultracold atom gases. Time evolution is also reflected in frequency-dependent information, e.g. as absorption spectra and inelastic scattering cross-sections, or through the measurement of transport properties. As most of these many-body systems are not amenable to analytical treatment, a large effort has been devoted to developing numerical algorithms for the time evolution of quantum many-body systems.

In the case of low-dimensional systems, tensor networks [1–6] have established themselves as a very powerful descriptive framework. Tensor network algorithms have been proposed which work directly in frequency space [7–15] and are typically used for the calculation of spectral functions. A large number of other tensor network methods work directly in real time [4, 6, 16–23]. Frequency-dependent information can then be obtained by Fourier transformations [19]. Most applications have been in the special case of matrix product states. In this paper we will present calculations based both on matrix product states and tree tensor network states.

The common limitation of all these methods is that they have difficulty in accessing long times or, equivalently, high frequency resolution. This is due to the entanglement barrier: in general, entanglement grows during time evolution. In the worst case, the bipartite von Neumann entanglement entropy S is upper-bounded as

$$S(t) \leq S(0) + a^{-1}vt, \quad (1)$$

where v is a typical velocity scale of the system, such as the spin wave or Fermi velocity, and a a constant of unit length. As the required resources in tensor networks, typically measured by the bond dimension m , scale exponentially with the entanglement, $m \sim e^S$, [24, 25] the computational cost of time evolutions then grows exponentially in the worst case [24, 30] which drastically limits accessible times.

The worst-case scenario occurs for global quenches of systems. In many cases, however, one is rather interested in numerically more benign time-dependent correlation functions because they relate directly to experimental probes. In the case of zero-temperature calculations for a system with Hamiltonian \hat{H} , ground state $|\psi_0\rangle$ and ground state energy E_0 , they are generically given by

$$C_{OP}(t) = \langle \psi_0 | \hat{O}^\dagger(t) \hat{P} | \psi_0 \rangle \quad (2)$$

for two operators \hat{O} , \hat{P} , where in many applications $\hat{O} = \hat{P}$. The time evolution of operators is given by

$$\hat{O}(t) = e^{+i(\hat{H}-E_0)t} \hat{O} e^{-i(\hat{H}-E_0)t}. \quad (3)$$

Here, entanglement growth is typically logarithmic in t , [28, 31] leading to a power-law growth of the required resources. While this increases accessible times, these times and hence the achievable frequency resolution are still quite limited. This is a particular problem if one is especially interested in (very) low frequency behavior, which is often the case in solids.

Since their invention, time-evolution methods for tensor networks have also been frequently used on the imaginary axis, for instance for ground-state searches. This reflects the fact that imaginary time evolution generally

* martin.grundner@physik.uni-muenchen.de

acts as a gradual energy truncation: it suppresses high-energy states and enhances low-energy states exponentially in the long-time limit [4]. Entanglement growth does not act as a limiting factor. So far, energy truncation algorithms have only been combined successfully with tensor network methods that calculated correlation function directly in frequency space [11, 13]. Imaginary-time evolution methods for tensor networks have also been successfully employed in the context of dynamical mean-field theory (DMFT) and related embedding methods [32–34] giving access to realistic multiband models, but with limited reliable information on low-frequency behavior [35–38]. Related real-time methods for DMFT have made good progress over the last years [39–42] but realistic materials with multiband physics are very challenging and frequency resolution is limited by finite simulation times due to entanglement growth.

The goal of this paper is to combine real and imaginary time evolutions in the complex plane in order to develop methods to extract real-time information while using imaginary-time evolution to limit the growth of entanglement during time evolution. This leads to much faster, less resource-intensive calculations which in turn give cheaper access to the same information as real-time evolutions or allow one to proceed to longer times and better frequency resolution. Note that the idea of complex time evolution has been recently discussed in the context of Quantum Monte Carlo simulations [43]. Similar ideas are also published in another work [44].

We introduce contours in the complex plane as $z(t) = t + i\tau(t)$ and extend the definition of $C_{OP}(t)$ as

$$C_{OP}(z) = \langle \psi_0 | \hat{O}^\dagger(z) \hat{P} | \psi_0 \rangle, \quad (4)$$

where

$$\hat{O}(z) = e^{+i(\hat{H}-E_0)z} \hat{O} e^{-i(\hat{H}-E_0)\bar{z}} \quad (5)$$

with \bar{z} the complex-conjugate of z . Effectively, then

$$C_{OP}(z) = \langle \psi_0 | \hat{O}^\dagger e^{-i(\hat{H}-E_0)\bar{z}} \hat{P} | \psi_0 \rangle. \quad (6)$$

Any discussion of possible contours in the complex plane cannot be exhaustive; we present easily implemented contours for which reliable post-processing methods exist to extract the desired real-time result. The various schemes allow mutual verification, and present a different balance of speed vs precision. We first focus on the single-impurity Anderson model (SIAM) as a test case for which extremely precise data is available, also within the framework of tensor network methods. After establishing benchmark data (Sec. II), we introduce two main classes of contours: a contour parallel to the real axis (Sec. III) and a tilted contour inclined with respect to the real axis (Sec. IV). The results from these contours all have to be post-processed, for which we present various approaches; we will denote the resulting methods by “contour used (post-processing approach)”. We show results both for the impurity spectral function and for

the numerically challenging calculation of the self-energy at very low frequencies, down to the Fermi liquid regime where $\text{Im}\Sigma(\omega) \sim \omega^2$. An additional procedure is based on a kink contour; it requires no post-processing at all, but has to be controlled for numerical instability; it is discussed in Appendix D, but not used in the main text. All methods exhibit a substantial speed-up and provide accurate results. The methods are robust and cheap. Furthermore, unlike in [44], our methods do not require to calculate powers of the Hamiltonian, a task which may prove difficult for multiband systems. We further illustrate our method on the example of a model with three impurity orbitals that interact via a Hubbard–Kanamori or a Dworin–Narath interaction (Sec. V). We show that even the calculation of the self-energy at very low frequencies can be achieved in the three-band case, with a quality comparable to the Numerical Renormalization Group (NRG) [45–47]. We therefore expect that our methods are also applicable in realistic calculations for multiband materials.

II. BENCHMARK MODEL: SIAM

The first test case for the usefulness of the various complex time-evolution schemes is the retarded impurity Green’s function and the associated impurity spectral function of the single impurity Anderson model (SIAM). The SIAM is a prototypical model describing magnetic impurities in metals [48] that features low energy structures that are well understood both numerically [45–47, 49] and analytically [48, 50].

The Hamiltonian of the SIAM is given by $\hat{H} = \hat{H}_{\text{imp}} + \hat{H}_{\text{bath}}$ with

$$\hat{H}_{\text{imp}} = U \hat{n}_{0\uparrow} \hat{n}_{0\downarrow} + \epsilon_0 (\hat{n}_{0\uparrow} + \hat{n}_{0\downarrow}), \quad (7)$$

$$\begin{aligned} \hat{H}_{\text{bath}} = & \sum_{k=1}^{N_b} \sum_{\sigma} (v_{0,k\sigma} \hat{c}_{k\sigma}^\dagger \hat{c}_{0\sigma} + v_{0,k\sigma}^* \hat{c}_{0\sigma}^\dagger \hat{c}_{k\sigma}) \\ & + \sum_{k=1}^{N_b} \sum_{\sigma} \epsilon_{k\sigma} \hat{n}_{k\sigma}, \end{aligned} \quad (8)$$

where $\hat{c}_{k\sigma}^\dagger$ ($\hat{c}_{k\sigma}$) are fermionic creation (annihilation) operators with spin $\sigma \in \{\uparrow, \downarrow\}$. The impurity site is located at $k = 0$. $\hat{n}_{k\sigma}$ are density operators and U is the Coulomb repulsion strength. ϵ_0 is chosen as $-U/2$; the model is at half-filling. The on-site potentials $\epsilon_{k\sigma}$ and the impurity-bath hopping elements $v_{0,k\sigma}$ are obtained by discretizing the hybridization function $\Delta(\omega)$. For our calculations we use a semi-elliptical hybridization function defined as

$$-\frac{1}{\pi} \text{Im}\Delta(\omega) = \frac{D}{2\pi} \sqrt{1 - \left(\frac{\omega}{D}\right)^2}, \quad (9)$$

for $\omega \in [-D, D]$, where D represents the half-band width. The support of the hybridization function is discretized

linearly into an odd number of equally sized intervals; see [47, 51] for details of this discretization procedure. For simplicity, we will drop all spin indices in the following.

The $T = 0$ retarded impurity Green's function is, without spin indices, given by

$$G(t) = -i\theta(t) \langle \psi_0 | \{ \hat{c}_0(t), \hat{c}_0^\dagger \} | \psi_0 \rangle, \quad (10)$$

where $|\psi_0\rangle$ is the ground state of the SIAM with energy E_0 . A Fourier transformation yields

$$G(\omega) = \int_0^\infty e^{i\omega t} e^{-\eta t} G(t), \quad (11)$$

where η is the usual damping factor. By definition, the impurity spectral function is then given by

$$\mathcal{A}(\omega) = -\frac{1}{\pi} \text{Im} G(\omega). \quad (12)$$

The calculation of $G(t)$ requires a real-time evolution. For time-independent Hamiltonians as here the problem of entanglement growth in the calculation of time-dependent correlators by matrix product state methods can be reduced by exploiting the homogeneity in time [52, 53], e.g.

$$\langle \psi_0 | \hat{c}^\dagger(0) \hat{c}(t) | \psi_0 \rangle = \langle \psi_0 | \hat{c}^\dagger(-t') \hat{c}(t'') | \psi_0 \rangle, \quad (13)$$

where we have split $t > 0$ into $t = t' + t''$ with $t', t'' > 0$. This can be written as

$$\langle \psi_0 | \hat{c}^\dagger(0) \hat{c}(t) | \psi_0 \rangle = [\hat{c}(-t') | \psi_0 \rangle]^\dagger \hat{c}(t'') | \psi_0 \rangle. \quad (14)$$

The real-time evolution up to t has been split into two time evolutions up to $-t'$ and t'' , respectively, and a final overlap which also occurs in the original formulation. Optimal limitation of entanglement growth is typically achieved for a symmetric split $t' = t'' = t/2$. The following real-time calculations all use this symmetric split.

For the time evolution we used the two-site version of the Time-Dependent Variational Principle (2TDVP) [4, 6, 22]. All results were obtained using a time step of $\delta t = 0.2D^{-1}$ and a truncated weight (the sum of the discarded reduced density matrix eigenvalues) of $w_t = 10^{-11}$, which we checked to give a converged result; the MPS bond dimension is allowed to grow accordingly. Up to the maximum time of $t_{\max} = 90D^{-1}$ the calculations reached a maximum bond dimension of $m \sim 1500$ for $w_t = 10^{-10}$ and $m \sim 2700$ for $w_t = 10^{-11}$. We chose values $U/D = 2$ and as bath size $N_b = 59$, except when stated otherwise. In the Fourier transformation, we used $\eta = 0.001D$ for spectral functions, except if stated otherwise, and $\eta = 0$ for self-energies. All tensor network simulations were performed using the SYTEN toolkit [54].

III. CONTOUR AT CONSTANT IMAGINARY TIME: PARALLEL CONTOUR

We now turn to the first complex-time method, where time is evolved along a complex contour parallel to the

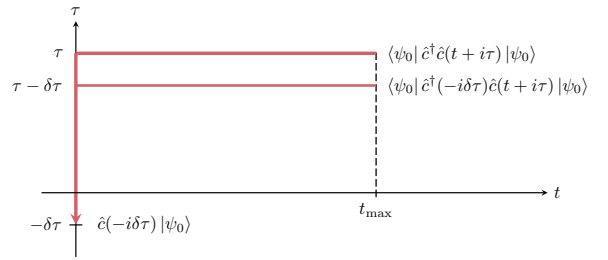


FIG. 1. Parallel contour $t + i\tau$. Multiple complex parallel contours are obtained with a small shift $\delta\tau$ from a first contour, cf. text.

real-time axis, i.e. at constant imaginary time, see Fig. 1. We have $z(t) = t + i\tau$ with $t \in [0, t_{\max}]$ and $\tau > 0$ constant. Here, z starts at 0, moves up to $i\tau$, and then continues from $i\tau$ to $t_{\max} + i\tau$. The entanglement growth with time is strongly limited compared the real time evolution, as illustrated in Fig. 13 in Appendix E, where we compare the time dependency of the entanglement for all the contours introduced in this paper. This contour suppresses high energy states aggressively, as reflected in the small entanglement growth at short times compared to other contours. It is therefore advantageous to use comparatively small $\tau > 0$ to retain a sufficient amount of high energy spectral weight.

An attractive feature of the parallel contour is that additional parallel contours offset by $\delta\tau$ can be obtained very cheaply from a first contour. Let us illustrate this point with one correlator

$$\begin{aligned} \langle \psi_0 | \hat{c}^\dagger \hat{c}(t + i(\tau + \delta\tau)) | \psi_0 \rangle \\ = [e^{-(\hat{H} - E_0)\delta\tau} \hat{c} | \psi_0 \rangle]^\dagger e^{i(\hat{H} - E_0)(t + i\tau)} \hat{c} | \psi_0 \rangle. \end{aligned}$$

We first compute the time evolution of the right ket up to time $t + i\tau$, and the additional time evolution $\delta\tau$ for the left bra, which is cheap to compute for small $\delta\tau$. Note that we can use positive or negative $\delta\tau$. In practice, we use $\delta\tau < 0$, as illustrated on Fig. 1. This allows us to obtain the correlations on a contour closer to the real axis, which is a priori harder to compute, at the price of a positive exponential evolution of the left term for a short time $\delta\tau$.

Let us introduce the complex-time spectral function \mathcal{A}_τ defined by

$$\mathcal{A}_\tau(\omega) \equiv \frac{1}{2\pi} \int dt e^{i(\omega + i\eta)t} \langle \psi_0 | \{ \hat{c}_0(t + i\tau), \hat{c}_0^\dagger \} | \psi_0 \rangle. \quad (15)$$

At $\tau = 0$, this function is the ordinary spectral function $\mathcal{A}_{\tau=0}(\omega) = \mathcal{A}(\omega) = -\frac{1}{\pi} \text{Im} G^R(\omega)$. Due to the simple form of the contour, we have an explicit relation between \mathcal{A}_τ and \mathcal{A} :

$$\mathcal{A}_\tau(\omega) = \mathcal{A}(\omega) e^{-\tau|\omega|} \quad (16)$$

which is established in Appendix A and exact in the limit $\eta \rightarrow 0$ as is used here. Our method consists simply

in computing $\mathcal{A}_\tau(t)$, then $\mathcal{A}_\tau(\omega)$ using a Fourier transform, and finally invert (16) to obtain the spectral function $\mathcal{A}(\omega)$. Despite its apparent simplicity, this inversion presents however two difficulties, both at low and high frequencies.

First, the inversion of (16) is clearly difficult at high frequencies, as small errors in $\mathcal{A}_\tau(\omega)$ are amplified by the exponential. Such errors may result from a too small t_{\max} for $\mathcal{A}_\tau(t)$ to be fully decayed, or from a broadening in the Fourier transform. This issue can be solved by introducing a cut-off frequency ω_c that limits the growth of the exponential factor as

$$\mathcal{A}(\omega) = \mathcal{A}_\tau(\omega)e^{\tau \min(|\omega|, \omega_c)}, \quad (17)$$

where ω_c is chosen such that it only acts in the high frequency tail of the spectral function. We found $\omega_c = 3D$ to yield overall good results in our calculations.

Second, the inversion of (16) is also difficult at low frequencies, even though the exponential term is close to 1. In this work, and in many physics applications, we are interested in a high precision computation of the behavior of the spectral function $\mathcal{A}(\omega)$ or the self-energy $\Sigma(\omega)$ at low frequencies. The difficulty comes from the kink in $\mathcal{A}_\tau(\omega)$ at $\omega = 0$ in Eq. (16), caused by $|\omega|$ in $e^{-\tau|\omega|}$. This is an exact feature, but as $\mathcal{A}(\omega)$ does not exhibit a kink at $\omega = 0$, this must be exactly compensated by a kink in $\mathcal{A}_\tau(\omega)$ at $\omega = 0$. The latter requires high-accuracy results from long-time evolutions where tensor network methods are limited. As a result, the compensation is imperfect.

Our solution of this issue uses a linear combination of a few $\mathcal{A}_{\tau_k}(\omega)$ computed on parallel contours $t + i\tau_k$ (as described above), which is designed to compensate the low frequency singularity introduced by the $e^{-\tau|\omega|}$ factor. Introducing some weights a_k , and defining the function

$$h(\omega) \equiv \sum_{k=1}^n a_k e^{-\tau_k |\omega|} \quad (18)$$

we have

$$\mathcal{A}(\omega)h(\omega) = \sum_{k=1}^n a_k \mathcal{A}_{\tau_k}(\omega). \quad (19)$$

We choose the weights a_k such that the function $h(\omega)$ is flat close to $\omega = 0$, i.e. we cancel the first powers of its low ω expansion:

$$\sum_{k=1}^n a_k = 1 \quad (20a)$$

$$\sum_{k=1}^n a_k \tau_k^l = 0 \quad (20b)$$

for $l = 1, \dots, n-1$. As h is close to 1 at low ω , $h(\omega) = 1 + O(\omega^n)$, we can now safely invert (19):

$$\mathcal{A}(\omega) = h^{-1}(\omega) \sum_{k=1}^n a_k \mathcal{A}_{\tau_k}(\omega). \quad (21)$$

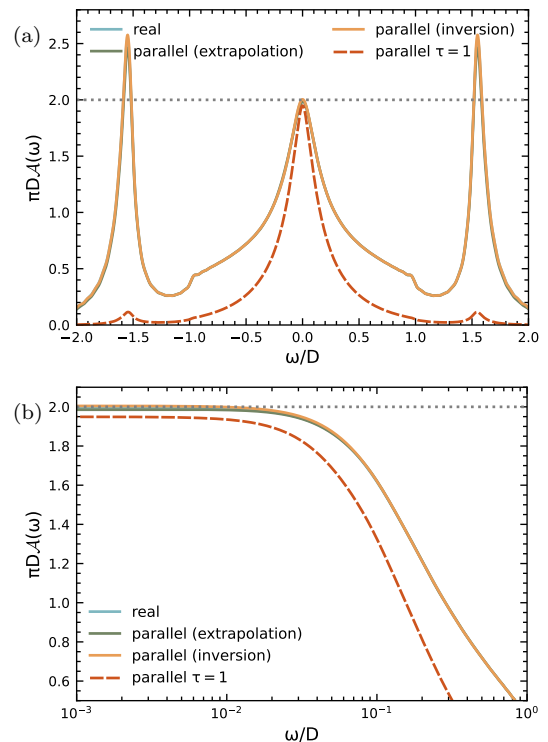


FIG. 2. (a) Comparison of spectral functions obtained on a parallel contour: "real" stands for the real-time reference data, $\tau = 1$ on the parallel contour without post-processing, parallel (extrapolation) and parallel (inversion) for the two methods of the main text. Nearly all spectral weight can be recovered by both methods in excellent agreement. The parallel (inversion) method used $n = 3$ with $\tau_k = 1, 1.15, 1.3$; the coefficients a_k (see text) are then approximately 33.2, -57.8, 25.6. The parallel (extrapolation) method used corrections to 6th order with 13 contours centered on $\tau = 1$ with a distance $\delta\tau = 0.075$. (b) Zoom at low frequencies with the same labels, showing the high accuracy of the parallel (inversion) and parallel (extrapolation) methods at very low frequencies.

In practice, we need to take τ_k which are neither too close (leading to large a_i that amplify numerical noise, due to the Vandermonde determinant in the linear system (20)), nor too distant as time-evolution errors affect precision. In this work, we used $n = 3$ and $\tau_k = 1, 1.15, 1.3$, if not stated otherwise. We will refer to this approach as the parallel (inversion) method.

Note that one can also perform a direct extrapolation to $\tau = 0$ using several parallel contours, which we call the parallel (extrapolation) method. We present it in Appendix B for completeness, but it turns out to be slightly inferior to the parallel (inversion) method. The parallel (extrapolation) method will be used in this paper as a check for the parallel (inversion) method.

Results. We present results of the spectral function of the benchmark SIAM in Figs. 2a and 2b. We use $\delta t = 0.2D^{-1}$, $w_t = 10^{-11}$, $N_b = 59$, $t_{\max} = 90D^{-1}$, and $\eta = 0.001D$. The simulation reached a maximum bond

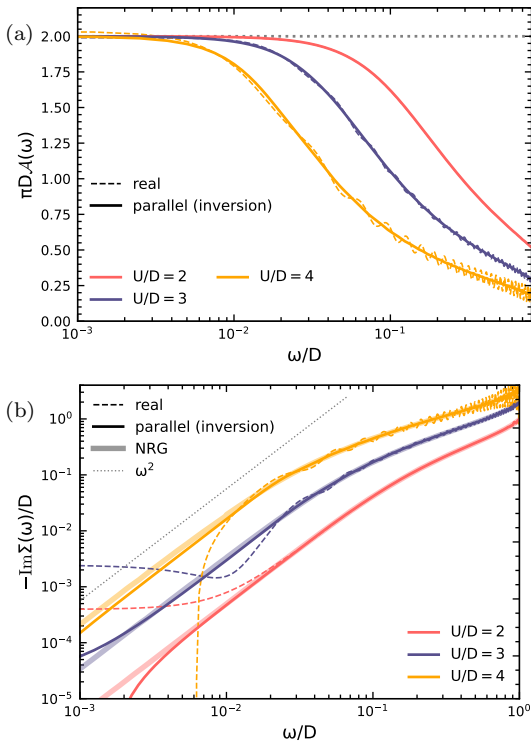


FIG. 3. (a) Spectral function of the SIAM for $U/D \in \{2, 3, 4\}$ with $N_b = 299$, using the $n = 2$ parallel (inversion) method with $\tau_k \in \{1.15, 1.3\}$; the coefficients are approximately $a_k \in \{8.6, -7.6\}$. We have an overall higher frequency resolution due to a finer bath discretization, zero broadening and a time evolution $t_{\max} \in \{150D^{-1}, 200D^{-1}, 250D^{-1}\}$. The maximum bond dimension is $m = 1500$ $SU(2)$ states. In all cases, in particular for larger U/D , the matching of the Friedel sum rule is less accurate for the real-time method. (b) Corresponding self-energies.

dimension of $m = 1023$. Both the parallel (inversion) and parallel (extrapolation) method provide spectral functions in excellent agreement with the much more costly (more than an order of magnitude) real-time benchmark data both at higher and in particular also at very low frequencies. The (generalized) Friedel sum rule $\pi D \mathcal{A}(0) = 2$ is matched to fractions of a percent. As both methods operate on the same numerical data, the parallel (extrapolation) method provides a cheap control of the quality of the spectral function. For Fig. 3a we use larger baths and a larger maximum bond dimension to calculate the spectral function for larger values of U/D both by real-time calculations and by the parallel (inversion) method. The Friedel sum rule is matched to very high accuracy in all cases; real-time results are much less accurate for larger U/D .

The determination of the self-energy $\Sigma(\omega)$ is numerically more challenging than that of the spectral function $\mathcal{A}(\omega)$. We calculate it from the Dyson equation $\Sigma(\omega) = G_0^{-1}(\omega) - G^{-1}(\omega)$, where $G_0(\omega)$ is the impurity Green's function for the non-interacting case. Its inverse is given by $G_0(\omega)^{-1} = \omega + i\eta - \epsilon_0 - \Delta(\omega)$ with $\eta = 0$ here.

We used the analytically known hybridization function. We obtain $G(\omega)$ from the parallel (inversion) method, which yields $\mathcal{A}(\omega)$, i.e. the imaginary part of $G(\omega)$. We then use the Kramers–Kronig rule to obtain the real part of $G(\omega)$.

To assess the quality of our self-energies, we henceforth include benchmark results from NRG. The NRG data was obtained in a state-of-the-art implementation [55–60] based on the QSpace tensor library [61], using a symmetric improved estimator for the self-energy [62]. The latter allows one to follow the imaginary part of the self-energy down to extremely low values of $|\text{Im}\Sigma|/D$.

As shown in Fig. 3b, the self energies calculated by complex time evolution reach the Fermi-liquid ω^2 -regime. The final breakdown at very low frequencies ($\omega/D \approx 0.007$) is due to small deviations from the sum rule and the use of Dyson's equation. We expect that the use of improved estimators [62] will alleviate this problem in future implementations. Before the breakdown, agreement with NRG results is excellent. Note that self-energies calculated from real-time results are much less accurate and plagued by unphysical oscillations.

IV. COMPLEX-TIME EVOLUTION AT FIXED ANGLE: TILTED CONTOUR

In our second complex-time approach, time is evolved along a complex contour tilted by various angles α with respect to the real axis, where $z(t) = t + it \tan \alpha$, i.e. $\tau = t \tan \alpha > 0$. We adapt the symmetric splitting of real-time evolutions to the complex plane by splitting $z = z' + z''$ with $z' = z'' = z/2$. Then we have

$$\langle \psi_0 | \hat{c}^\dagger(0) \hat{c}(z) | \psi_0 \rangle = [\hat{c}(-\bar{z}/2) | \psi_0 \rangle]^\dagger \hat{c}(z/2) | \psi_0 \rangle, \quad (22)$$

$$\langle \psi_0 | \hat{c}(z) \hat{c}^\dagger(0) | \psi_0 \rangle = [\hat{c}^\dagger(z/2) | \psi_0 \rangle]^\dagger \hat{c}^\dagger(-\bar{z}/2) | \psi_0 \rangle. \quad (23)$$

The two contours on which complex time evolution occurs now look as in Fig. 4.

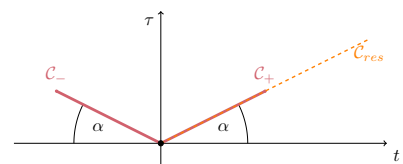


FIG. 4. Symmetrically split complex-time contour: Contour C_{res} from 0 to z is replaced by two symmetric contours C_+ and C_- from 0 to $z/2$ and $-\bar{z}/2$ respectively.

In all calculations, we use $\delta|z| = 0.2D^{-1}$, and again $w_t = 10^{-11}$ and $N_b = 59$. The maximum complex time is in all cases $|z|_{\max} = 90D^{-1}$, or real times $t_{\max} = 90D^{-1} \cos \alpha$. The resulting Green's function is Fourier transformed as

$$G_\alpha(\omega) = \int_0^\infty dt G_\alpha(t + i\tau) e^{i\omega t - \eta t} \quad (24)$$

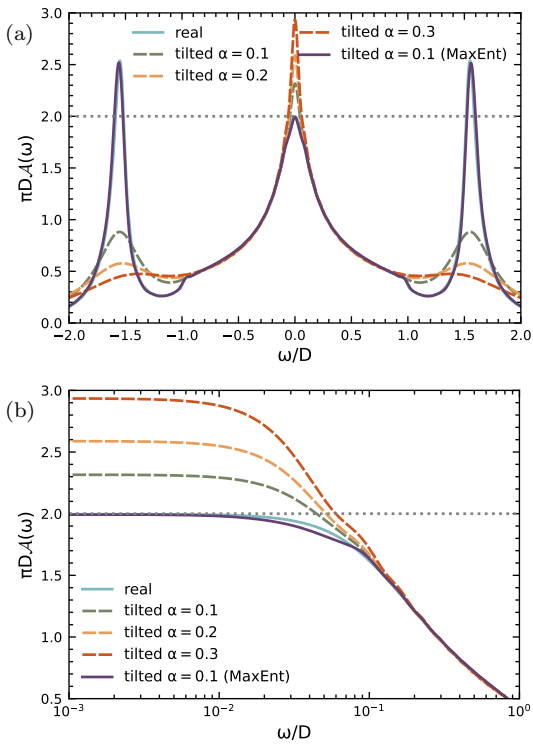


FIG. 5. (a) Comparison of spectral functions obtained on tilted contours with real-axis reference data ('real') and the tilted (MaxEnt) result from the tilted contour with $\alpha = 0.1$. The kink at $\omega/D = \pm 1$ is model specific. The dashed lines are data before post-processing. (b) shows the spectral functions of (a) and $\mathcal{A}(\omega)$ obtained after a MaxEnt continuation of $G_{0,1}(z)$ on a logarithmic frequency scale for $\omega/D > 0$ in $[10^{-3}, 10^0]$.

(again with $\eta = 0.001D$); the subscript α indicates that we evaluate on a tilted contour. The spectral function $\mathcal{A}(\omega)$ is then extracted as $\mathcal{A}_\alpha(\omega) \equiv -(1/\pi)\text{Im}G_\alpha(\omega)$. Results are shown on a linear and a logarithmic frequency scale in Fig. 5. Note that we do not expect to obtain the correct $\mathcal{A}(\omega)$ for $\alpha \neq 0$, as \mathcal{A}_α is just an intermediate step in the computation. Nevertheless, we find that peak positions in \mathcal{A}_α are well preserved for moderate angles thus still allowing for a rough interpretation of quasi-particle peaks, see Fig. 5a. We find a significant reduction in the entanglement entropy for all angles that can be understood as the result of damping the statistical weight of high energy states, as it is reflected in a reduction in the time-dependent energy expectation value of the system, see Fig. 6. The dampened growth in the entanglement entropy leads to a speed-up of a factor of the order 100 in the SIAM model for the specified parameters compared to our real-time reference calculation. This is reflected in the very small final bond dimensions, $m = 52$ for $\alpha = 0.3$, $m = 66$ for $\alpha = 0.2$ and $m = 137$ for $\alpha = 0.1$.

In order to compute the spectral function $\mathcal{A}(\omega)$, the data has to be post-processed, in this case by an analytical continuation of the complex-time data to the real axis by MaxEnt, yielding the tilted (MaxEnt) method;

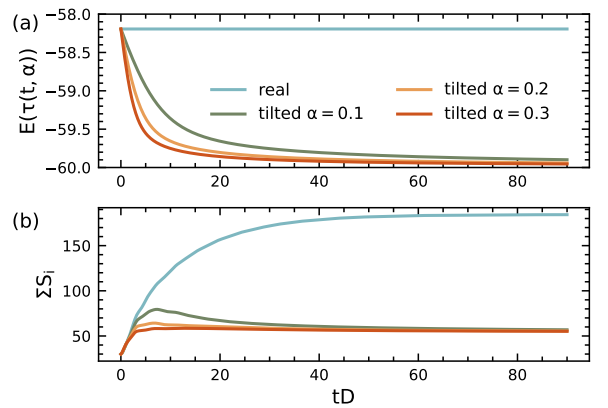


FIG. 6. Energy (a) and entanglement entropy (b) during time-evolution for $U/D = 2$. Imaginary time evolution along a tilted contour shifts the energy expectation value of the time-evolving state towards the ground state energy. Entanglement entropy, here given by the sum of the entanglement entropies for all system cuts, is reduced strongly along the tilted contours resulting in substantial speed-ups.

see App. C for a detailed discussion of MaxEnt. The agreement with the real-time data is overall very good and the Friedel sum rule obeyed to 0.4%, but there are small, but noticeable deviations from the true $\mathcal{A}(\omega)$ between $\omega/D \sim 10^{-2}$ and $\omega/D \sim 10^{-1}$ (Fig. 5b). As the analytic continuation kernel is generally ill-conditioned and its current formulation leads to deviations around the Fermi edge, this is not surprising. In comparison to the parallel (inversion) and parallel (extrapolation) methods, accuracy is lower for the tilted (MaxEnt) method, in particular at low frequencies. The tilted (MaxEnt) method is however the fastest, so may be very useful in DMFT applications for the intermediate steps of the iteration procedure. Note that the tilted contour can also be combined with the extrapolation scheme of Appendix B to yield the tilted (extrapolation) method; results will be shown for the self-energies calculated in the following section.

V. THREE-BAND MODEL CALCULATIONS

The need for reliable high-performance calculations of low-frequency information is particularly pressing for multi-orbital models used in realistic quantum embedding computations of strongly correlated materials [32–34], more specifically for transport computations. Accurate real frequencies quantum impurity solvers are rare, with the notable exception of NRG, which is however limited in the number of orbitals. In order to benchmark our method in such a case, we use the three-band Anderson model with the Hubbard–Kanamori interaction, which

reads

$$\begin{aligned}
\hat{H}_K = & U \sum_m \hat{n}_{m\uparrow} \hat{n}_{m\downarrow} + U' \sum_{m \neq m'} \hat{n}_{m\uparrow} \hat{n}_{m'\downarrow} + \\
& + (U' - J) \sum_{m < m', \sigma} \hat{n}_{m\sigma} \hat{n}_{m'\sigma} - J \sum_{m \neq m'} \hat{d}_{m\uparrow}^\dagger \hat{d}_{m\downarrow} \hat{d}_{m'\downarrow}^\dagger \hat{d}_{m'\uparrow} \\
& + J \sum_{m \neq m'} \hat{d}_{m\uparrow}^\dagger \hat{d}_{m\downarrow}^\dagger \hat{d}_{m'\downarrow} \hat{d}_{m'\uparrow}
\end{aligned} \quad (25)$$

where m, m' run from 1 to 3, U and U' are the intra- and inter-orbital Hubbard interaction, and J is the Hund's coupling. $\hat{d}_{m\sigma}$ and $\hat{d}_{m\sigma}^\dagger$ are fermionic annihilation and creation operators on band m . For the sake of consistency with real material calculations, we choose $U' = U - 2J$ [63]. Each impurity couples to a bath as in the SIAM. While it is not the most generic case (which would have non-diagonal bath couplings), we expect our approach to generalize without major difficulty.

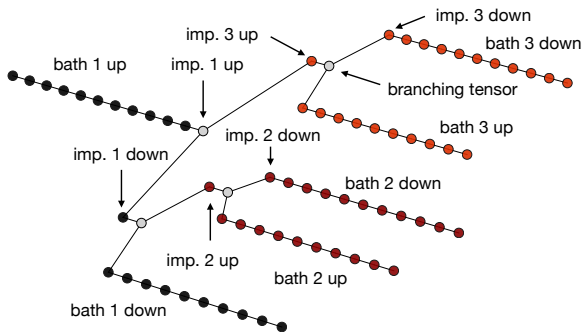


FIG. 7. T3NS for three-orbital calculations: The physical basis of all 3 impurities and their associated bath sites are split into spin-up and spin-down representations (empty or occupied). The resulting 6 (spinless) impurity orbitals are connected by branching tensors. The bath sites are attached as MPS-like chains.

As density of states we use the same semi-circular density of states as before and obtain the bath parameters as for the SIAM. Each bath is modeled by $N_b = 99$ bath sites, if not stated otherwise. As interaction parameters we consider $U/D = 2$ and $J/D = 0.3$. In all calculations, we set $\eta = 0$.

The simulations are carried out using 2TDVP until $t = 20D^{-1}$ and 1TDVP until the final time of $t = 180D^{-1}$. We use a tree tensor network, more specifically a T3NS [64] where trees are constructed only of rank-three tensors. These are either branching tensors with three legs establishing a tree geometry or physical tensors identical to matrix-product state tensors with two auxiliary connecting legs and one physical leg carrying the physical degrees of freedom (see Fig. 7). This representation is more adequate to multiorbital impurity problems and contains the fork geometry of [42] as a special case without the need of numerically costly four-leg tensors. The TDVP implementation follows [65].

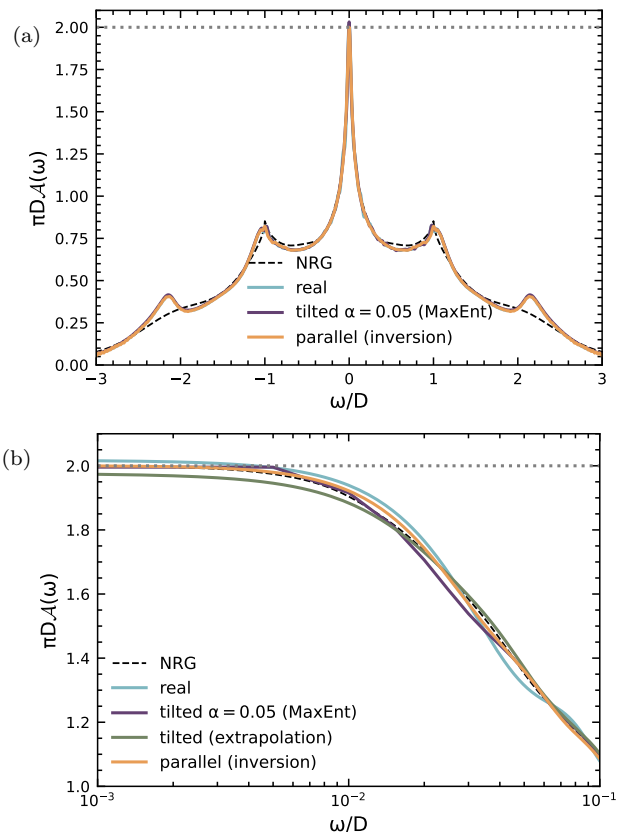


FIG. 8. Spectral function $\mathcal{A}(\omega)$ for a three-orbital model with Hubbard–Kanamori interaction. All calculations are at truncated weight $w_t = 10^{-10}$ and without broadening ($\eta = 0$). Real-time results stem from a time evolution up to $t_{\max} = 120D^{-1}$ with a maximum bond dimension $m = 1024$. For the tilted (MaxEnt) method at angle $\alpha = 0.05$ the corresponding values are $t_{\max} = 180D^{-1}$ and $m = 2048$, for the parallel (inversion) method at $\tau = 1$, $t_{\max} = 220D^{-1}$ and $m = 1024$; in that case, an increased bath size $N_b = 139$ was used. The post-processing for the parallel (inversion) method used $n = 3$ contours at $\tau_k \in \{1, 1.15, 1.3\}$ with coefficients $a_k \in \{33.2, -57.8, 25.6\}$ (rounded). The Friedel sum rule is obeyed to an accuracy of 0.2% for the tilted (MaxEnt) data and 0.02% for the parallel (inversion) data versus 0.8% in the real-time calculation. (b) zoom into Fig. (a) with additional data obtained from the tilted (extrapolation) method using contours $\alpha \in [0.05, 0.1, 0.15, 0.2, 0.25, 0.3]$, averaging over all 4th order contributions. The oscillations in the real-time result are now clearly visible. The tilted (MaxEnt) result using $\alpha = 0.05$ shows a similar unphysical slight dip between $\omega/D = 10^{-2}$ and 10^{-1} as for the SIAM.

We again use NRG results as a benchmark, since it is currently the most accurate method available for low frequencies. The Hubbard–Kanamori Hamiltonian in its band-degenerate form has an $SO(3)$ orbital symmetry which makes it accessible to standard multiorbital NRG [66–69] (without the need for interleaving the Wilson chain [69–73]). Note that we do not exploit the $SO(3)$ orbital symmetry in our T3NS calculations as it typically does not appear in multiorbital simulations of real materials.

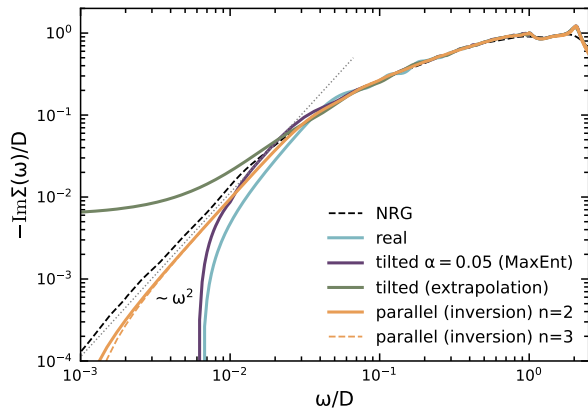


FIG. 9. Imaginary part of the self-energy of the Hubbard–Kanamori Hamiltonian. The real-time result (“real”) shows oscillations and fails at $\omega/D \approx 0.05$, missing the low-frequency physics. The dotted line indicates the ω^2 Fermi-liquid behavior of the self energy. The tilted (MaxEnt) and tilted (extrapolation) methods do not reach this regime. The parallel (inversion) method (with $n = 2, 3$ with $\tau_k \in \{1.15, 1.3\}$ and $a_k \in \{8.7, -7.7\}$) is in very good agreement with NRG data but for a prefactor (see text) down to $\omega/D \approx 0.002$.

Despite the tailored representation on a tree-tensor network, pure real-time calculations fail at high frequency resolution. The complex-contour calculations, on the other hand, yield reliable results. In Figs. 8a and 8b we show that the spectral function results from the tilted (MaxEnt) method and from the parallel (inversion) method agree overall very well, whereas the real-time results show unphysical wiggles. There is however again a small discrepancy between the tilted (MaxEnt) and the parallel (inversion) methods at ω/D a bit above 0.01; in view of the results below we interpret this as an inaccuracy of the tilted (MaxEnt) result. NRG results agree excellently at low frequencies, but show the expected deviations for larger frequencies due to the logarithmic discretization of NRG.

We calculate the self-energy of the Hubbard–Kanamori Hamiltonian as in the case of the SIAM, but add further methods to have some mutual benchmarking. We obtain $G(\omega)$ in four different ways: (i) from a real-time calculation; (ii) from a tilted (MaxEnt) calculation at $\alpha = 0.05$; (iii) from a tilted (extrapolation) calculation; and (iv) from a parallel (inversion) calculation at $\tau = 1.3$. In cases (ii) and (iv), we obtain $\mathcal{A}(\omega)$ and then $\text{Im}G(\omega)$ with the Kramers–Kronig transformation.

In Fig. 9, we observe that the real-time result shows weak, but unphysical oscillations at frequencies above $\omega/D \approx 0.05$ and fully misses the low-energy Fermi-liquid physics $\text{Im}\Sigma(\omega) \sim \omega^2$ at lower frequencies. Both the tilted (MaxEnt) and tilted (extrapolation) methods perform somewhat better, but also fail at low frequencies. At higher frequencies, the tilted (extrapolation) result is in perfect agreement with the parallel (inversion) result.

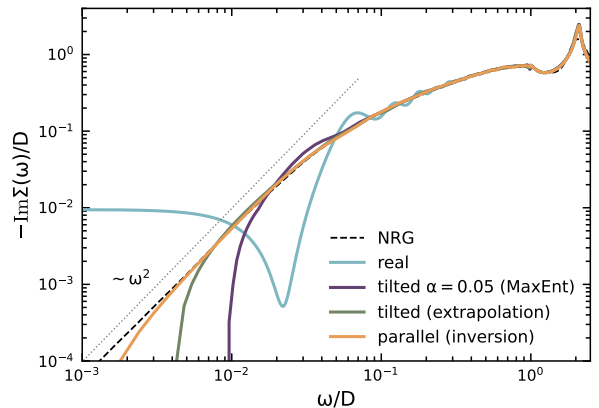


FIG. 10. Imaginary part of the self-energy of the Dworin–Narath Hamiltonian. The parallel (inversion) method is in very good agreement with NRG data down to $\omega/D \approx 0.004$. All calculations are at truncated weight $w_t = 10^{-10}$. Real-time evolution is up to $t_{\text{max}} = 120D^{-1}$ with a maximum bond dimension $m = 512$. The tilted (MaxEnt) method uses angle $\alpha = 0.05$ and goes to $t_{\text{max}} = 180D^{-1}$ and maximum bond dimension $m = 1024$, the parallel (inversion) method uses $\tau = 1$ and goes to $t_{\text{max}} = 140D^{-1}$ and maximum bond dimension $m = 1500$, the bath size was increased to $N_b = 139$. Results for the parallel (inversion) method are shown for $n = 4$ with $\tau_k \in \{0.85, 1, 1.15, 1.3\}$; the coefficients a_k (see main text) are then approximately $\{9.8, -14.2, 7.5, -2.1\}$.

The parallel (inversion) method easily reaches the ω^2 -regime. As in the case of the SIAM, sum rule violations in connection with the use of Dyson’s equation lead to a breakdown at very low frequencies. Interestingly, the breakdown does not occur at higher frequency than in the SIAM case, indicating that this problem is not aggravated by the higher complexity of the model studied.

In the case of the three-band Hubbard–Kanamori model, NRG provides the best results for comparison but is no longer an *exact* benchmark: The large dimension of the local Hilbert space requires a rather large value of the discretization parameter, here $\Lambda = 6$ [47]. Averaging over n_z shifted discretization grids mitigates the effects of a coarse resolution of the hybridization function to some extent [57]. As discussed in Appendix F, we found the best results by extrapolating to $n_z \rightarrow \infty$. Generally, we observe that the NRG result for the ω^2 coefficient of $-\text{Im}\Sigma$ decreases with increasing resolution of the hybridization function (decreasing Λ , increasing n_z). It is therefore remarkable that the T3NS result is slightly offset from the NRG result by a factor < 1 in the ω^2 regime before the breakdown occurs at $\omega/D \approx 0.002$.

We also considered the Dworin–Narath Hamiltonian, which can be represented similarly as in Eq. (25), except that one necessarily has $U' = U - J$ and that the last term in Eq. (25) (known as pair hopping) is missing [63]. It obeys a larger orbital symmetry than the Hubbard–Kanamori Hamiltonian (SU(3) instead of SO(3)), and thus allows for highly accurate NRG calculations at $\Lambda = 4$ (see also Appendix F). Figure 10 shows

the imaginary part of the self-energy for the Dworin–Narath Hamiltonian with the same parameters as before ($U/D = 2$ and $J/D = 0.3$). The performance of the time-evolution methods is similar to Fig. 9: going toward low frequencies, the real-time evolution soon yields unphysical results, the tilted (MaxEnt) and tilted (extrapolation) schemes improve on this, while the best result by far is obtained via the parallel (inversion) method. The corresponding curve follows the Fermi-liquid ω^2 behavior down to $\omega/D \approx 0.004$. Importantly, the agreement with NRG is excellent, as the coefficients of the ω^2 behavior match. This indicates that the small difference in the prefactor of the self-energy in Fig. 9 comes from the fact that the Hubbard–Kanamori NRG result is not fully converged in all numerical parameters.

The parallel (inversion) method emerges as the most reliable and performing among the methods tested here. Moreover, it can be further improved systematically: it rests on an analytically exact formula and the breakdown at very low frequencies occurs because $G(t + i\tau)$ was not calculated for long enough times to yield highly reliable $G_\tau(\omega)$ for very small ω . As entanglement growth is curtailed, the region of ω^2 scaling can be extended to smaller frequencies by longer time evolutions. Note that the complex-time evolutions employed here easily generalize to less symmetric situations, as we did not use any of the emerging larger symmetries, and also have sufficient numerical efficiency to move to systems with more than three orbitals. Additionally, we expect that the accuracy of the self-energies provided by complex time evolution can be further improved by using improved estimators as in NRG [62].

VI. CONCLUSION

Complex-time evolution is an addition to the toolbox of tensor network simulations that offers high resolution when computing Green’s functions at low frequencies at a fraction of the computational cost. At the same time, it maintains the quality of high-frequency data previously available. The speedup is highest for the tilted contour, about two orders of magnitude. MaxEnt as a method of analytical continuation provides very good, but not excellent agreement with real-time data where the latter is essentially exact.

The parallel contour calculations yielded the second highest speedup of (more than) an order of magnitude; post-processing by two different methods, inversion and extrapolation, provided excellent mutual agreement, allowing mutual control, as well as with benchmark data. Results were always somewhat more accurate than tilted (MaxEnt) results. In the very low frequency regime for the self-energy of the three-band model, our most challenging calculation, the tilted (extrapolation) method ran into difficulties, but the parallel (inversion) method was stable and accurate: The calculation of the self-energy of the Hubbard–Kanamori and Dworin–Narath three-

band models reaches successfully into the $\text{Im} \Sigma(\omega) \sim \omega^2$ Fermi liquid regime down to $\omega/D \approx 0.002$ in agreement with NRG benchmark results. The parallel (inversion) method therefore seems to provide the best compromise in speedup and accuracy. It can be systematically improved to reach even lower frequencies, albeit at mounting numerical cost; design decisions here will reflect compromises between required low-frequency resolution and available CPU time.

The availability of multiple complex time-evolution schemes that can be directly used or post-processed in different ways to extract real-time information makes these methods very controlled. We expect these methods to be particularly useful in the context of quantum-embedding methods using frequency-based information such as DMFT and its derivatives, where efficiency of impurity solvers is paramount. In fact, the very high efficiency of the tilted contour calculations may make them the preferred approach for DMFT despite the limited accuracy. It remains as a challenge for the future to apply these methods in the context of global quenches or higher-dimensional systems simulated directly on their real-space lattices. It is hoped that the suppression of high-energy contributions by imaginary time evolution may give access to long-time information inaccessible to real-time methods without substantial loss of accuracy.

VII. ACKNOWLEDGMENTS

We acknowledge useful discussions with Xiaodong Cao, Sebastian Paeckel and Miles Stoudenmire. M.G. and U.S. acknowledge support by the Deutsche Forschungsgemeinschaft (DFG, German Research Foundation) under Germany’s Excellence Strategy-426 EXC-2111-390814868. M.G. and U.S. thank the Flatiron Institute for its hospitality. The Flatiron Institute is a division of the Simons Foundation.

Appendix A: Proof of Eq. (16)

Using the definition of the complex time evolution (5) we obtain

$$\begin{aligned} \langle \psi_0 | \{ \hat{c}_0(z(t)), \hat{c}_0^\dagger \} | \psi_0 \rangle &= \sum_A |\langle \psi_0 | \hat{c}_0 | A \rangle|^2 e^{-iE_A(t-i\tau)} \\ &\quad + |\langle \psi_0 | \hat{c}_0^\dagger | A \rangle|^2 e^{+iE_A(t+i\tau)} \end{aligned}$$

where $|A\rangle$ is a eigenstate basis of the many-body Hamiltonian $H - E_0$, and E_A its eigenvalue. From the definition of \mathcal{A}_τ (15), we have

$$\begin{aligned} \mathcal{A}_\tau(\omega) &= \sum_A |\langle \psi_0 | \hat{c}_0 | A \rangle|^2 \delta(\omega - E_A) e^{-E_A \tau} + \\ &\quad |\langle \psi_0 | \hat{c}_0^\dagger | A \rangle|^2 \delta(\omega + E_A) e^{-E_A \tau} \end{aligned}$$

in the limit $\eta \rightarrow 0$. By definition of the ground state, $E_A > 0$. In the first term, $\omega = E_A = |\omega|$, while in the second term $E_A = -\omega = |\omega|$, so we get

$$\mathcal{A}_\tau(\omega) = e^{-|\omega|\tau} \sum_A |\langle \psi_0 | \hat{c}_0 | A \rangle|^2 \delta(\omega - E_A) + |\langle \psi_0 | \hat{c}_0^\dagger | A \rangle|^2 \delta(\omega + E_A)$$

and therefore

$$\mathcal{A}_\tau(\omega) = \mathcal{A}_{\tau=0}(\omega) e^{-|\omega|\tau}$$

Appendix B: Extrapolation Method

We assume that we know n Green's functions $G(t+i\tau_k)$ for n different τ_k . As seen previously, they can be generated at low numerical cost from a single contour. We approximate the behavior by a power series incorporating terms up to order $n-1$,

$$G(t+i\tau) = G(t) + \sum_{m=1}^{n-1} \tau^m h_m(t). \quad (\text{B1})$$

For n values τ_k , we have n equations with n unknown variables, the Green's function $G(t)$ we are interested in and $n-1$ coefficients $h_m(t)$ which we will not require explicitly. This linear equation system can be written as $\mathbf{g} = \mathbf{M} \cdot \mathbf{h}$, where the vector components are $g_k = G(t+i\tau_k)$, $h_0 = G(t)$ and $h_k = h_k(t)$ for $k > 0$, and

$$M_{kl} = \tau_k^{l-1}. \quad (\text{B2})$$

An inversion of \mathbf{M} yields

$$G(t) = \sum_{k=1}^n (M_{1k})^{-1} G(t+i\tau_k). \quad (\text{B3})$$

For increasing n the inversion of \mathbf{M} becomes more difficult. To stabilize it, it is useful to re-scale both $h_k(t)$ and \mathbf{M} such that $G(t)$ remains unaffected. With τ_{\max} the largest τ_k , we re-scale as

$$M_{kl} = \left(\frac{\tau_k}{\tau_{\max}} \right)^{l-1}. \quad (\text{B4})$$

If we want to solve at order n , but know $G(t+i\tau_k)$ for more than n different τ_k , we found a substantial increase of accuracy by averaging over all different n th-order extrapolations with different choices of n values of τ_k . In practice, we used $n=6$ for 13 different $G(t+i\tau_k)$. In the calculations shown here (Figs. 2a and 2b), they were equidistantly ($\delta\tau = 0.075$) centered on $\tau = 1$. (Note that the extrapolation method can also be applied to the linear contours of Sec. IV.)

Appendix C: Analytic Continuation

For the analytical continuation by MaxEnt, we follow the procedure outlined in [43]. There is a connection between $G(z)$ and the spectral function \mathcal{A} in the case of complex-time contours, given by

$$G(z) = -i\Theta(t) \int_{-\infty}^{\infty} d\omega \mathcal{A}(\omega) K(z, \omega), \quad (\text{C1})$$

where the integration kernel $K(z, \omega)$ is defined as

$$K(z, \omega) = \begin{cases} \exp(-i\bar{z}\omega), & \text{if } \omega \geq 0 \\ \exp(-iz\omega), & \text{if } \omega < 0 \end{cases}$$

As the kernel may be complex valued, the equations have to be slightly adapted [43]. Besides this, the well established methods of MaxEnt were used [74, 75]. We found analytic continuation to be rather stable with this kernel. However, care must be taken at low frequencies as the kink of the kernel at zero frequency leads to results deviating from spectral functions obtained from purely real-time evolution. We propose two different measures as possible resolutions. First, we use a broadening around the discontinuity, by replacing the problematic $\text{sgn}(\omega)$ with $\tanh(\omega/\sigma)$, with the free factor σ . The kernel then reads

$$K(z, \omega) = \exp(-(it + \tanh(\omega/\sigma)\tau)\omega) \quad (\text{C2})$$

In the limit $\sigma \rightarrow 0$ this kernel is exact. Hence, σ has to be chosen sufficiently small to leave the overall structure of the inversion problem unchanged. We found sensible values to be smaller than the width of the main peak, at $\sigma = 0.11$. Although this change helps a bit, we found it to be not very reliable, leading to strong oscillations around $\omega = 0$. We therefore implemented a second method, which introduces a correction term to $Q(\mathcal{A}) = -\chi^2 + S(\mathcal{A})$, maximized in normal MaxEnt. We rather take

$$Q(\mathcal{A}) = -\chi^2 + \alpha S(\mathcal{A}) - \beta \int_{-\infty}^{\infty} d\omega \left(\frac{d\mathcal{A}}{d\omega} \right)^2 f(\omega). \quad (\text{C3})$$

The additional last term favors smooth spectral functions, since, when maximizing Q , it tries to minimize the quadratic slope of \mathcal{A} . The observed quick oscillations around zero are thus smoothed out, since they increase the quadratic slope. $f(\omega)$ serves as a weighting factor focusing on small frequencies. We used a Gaussian $f(\omega) = \exp(-(\omega/\sigma)^2)$. The new parameter β controls this correction term; $\beta = \alpha$ turned out to be a viable choice. For all MaxEnt calculations involving the three-band model, we chose $\sigma = 1$. The MaxEnt with correction term maintains the correct peak heights. We leave an even better stabilization of the Kernel at low frequencies to further research.

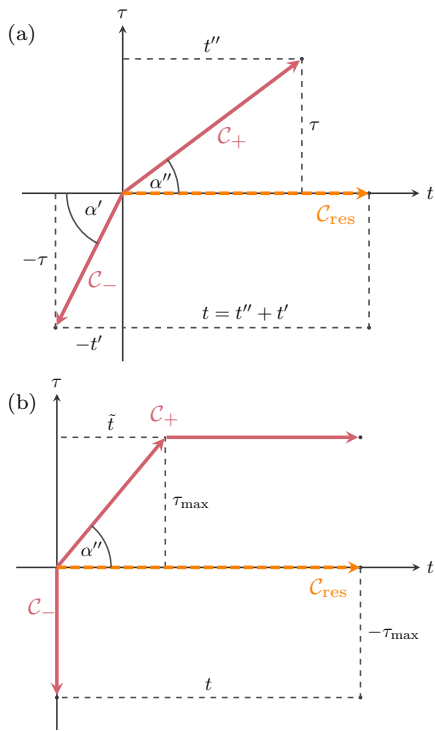


FIG. 11. (a) Contour for complex time evolution with no postprocessing. (b) Stable version with a horizontal contour, Cf Text.

Appendix D: Real Frequency Results Without Analytic Continuation: Kink contour

For an additional approach, we reformulate the idea of time splitting in the complex plane in a different way by splitting *real* time into two *complex* times via $t = z' + z''$ with $z' = t' - i\tau$, $z'' = t'' + i\tau$, $t, t', t'', \tau > 0$ where $t = t' + t''$. Then

$$\langle \psi_0 | c^\dagger(0)c(t) | \psi_0 \rangle = [c(-\bar{z}') | \psi_0 \rangle]^\dagger c(z'') | \psi_0 \rangle \quad (\text{D1})$$

Note that in this case no analytical continuation or any other post-processing is required. If we continue to use linear contours in the complex plane, we get two contours \mathcal{C}_+ and \mathcal{C}_- in the upper right and lower left quadrants of the complex plane at angles α' and α'' which need not be identical as no symmetric splitting of t is required (see Fig. 11a). The two angles α', α'' can be chosen freely, but the imaginary time steps in \mathcal{C}_+ suppress the entanglement growth of the real-time evolution, whereas the same steps increase that entanglement growth on contour \mathcal{C}_- . This suggests a splitting where $\alpha' > \alpha''$ and hence $t' < t''$. In our calculations, we chose $\alpha'' = 0.1$ and $\alpha' = \pi/2$, i.e. a purely imaginary time evolution on a vertical contour \mathcal{C}_- ; $t = t''$ and $t' = 0$. Numerical instabilities in the time evolution on \mathcal{C}_- limit our maximum evolution time on the corresponding contour \mathcal{C}_+ to about $|z''| = 20D^{-1}$ or $\tau'' = 1.996D^{-1}$ for $\alpha'' = 0.1$ and $\alpha' = \pi/2$. The numerical instabilities in the time evolution on \mathcal{C}_- can be seen clearly in Fig. 12a. It might be suspected that the expo-

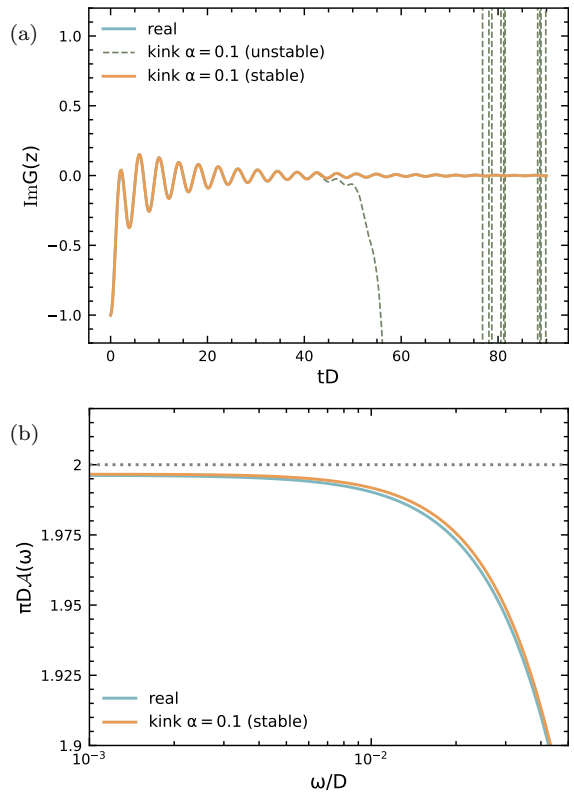


FIG. 12. Imaginary part of the retarded Green's function vs t and spectral function vs ω for the SIAM at $U/D = 2$ and other parameters as before, obtained using the kink contour method with $\alpha'' = 0.1$ and $\alpha' = \pi/2$. The "stable" label refers to the second contour in Fig. 11a with $t_{\max} = 20D^{-1}$ or $\tau_{\max} = 0.998 = 1.996D^{-1}$. The "stable" contour result is in excellent agreement with the real time reference data.

ponential growth of the weight of higher-energy states on contour \mathcal{C}_- suppresses the contribution from low-energy states which are enhanced on contour \mathcal{C}_+ and numerical cancellations fail, leading to the instabilities. At the onset of the instabilities, the norm difference is only of the order 10^4 , which should only lose insignificant digits. So even though exponential growth will eventually make this method unstable, it does not seem to be the origin of the currently observed instabilities. We suspect that they are related to the relatively subtle interplay of errors in the TDVP method which suggests that improvements are possible at the level of the time-evolution method.

The instability is mended by continuing with a contour parallel to the real axis for larger times, before instabilities occur, see Figure 11b. Figure 12b shows the excellent quality of the result for the spectral function of the SIAM.

This method is at the moment the least performant in speed, roughly a speed-up of a factor three, but attractive due to the absence of post-processing. Methodological progress in the time-evolution methods may make it fully competitive.

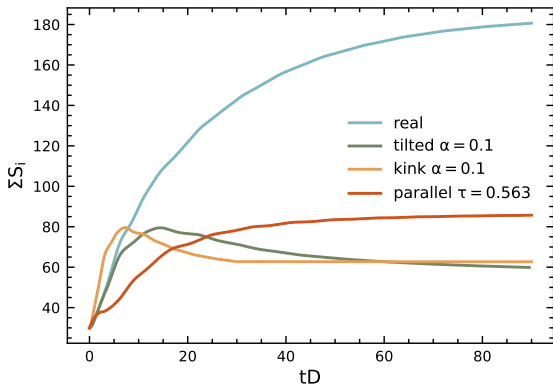


FIG. 13. Comparison of the entanglement entropy on different complex-time contours. As the system is heterogeneous, the sum of the entanglement entropies for all system cuts is shown. Kink $\alpha = 0.1$ is the post-processing free contour with vertical contour along the negative imaginary axis and a tilted contour in positive imaginary direction until $t = 30D^{-1}$ and $\tau = 0.563$ a parallel contour with constant imaginary part $\tau = 0.563$. Times of contours exploiting real-time splitting were multiplied by a factor 2 to represent the same final time.

Appendix E: Comparison of Contours

The ideal choice of the complex contour is ultimately reliant on the model and its specific high energy quasi-particle peak structure, because the loss of high-energy information is greater if the contour is further away from the real-time axis during early times. A second crucial aspect is the growth of entanglement entropies on the complex contours, as it determines the computational cost. This is illustrated on Fig. 13. Not surprisingly, the real-time contour has the strongest overall growth of entanglement, which does not saturate, explaining the vastly larger numerical resources required. The tilted contour (here $\alpha = 0.1$) starts with a similar growth of entanglement at early times when it is close to the real axis, but actually reveals even a slight decrease before saturation at some relatively small value. The kink contour without post-processing (kink $\alpha = 0.1$) has a very strong initial growth of entanglement, even stronger than for real-time evolution, because it does not exploit time-splitting in the real-time direction. Ultimately, though, entanglement strongly resembles that of the tilted contour, reminiscent of the observed saturation of entanglement growth for all complex-time contours. Finally, the parallel contour at constant τ has the slowest early growth of entanglement as it aggressively suppresses high-energy states, but then settles on a somewhat larger saturation value as the contour stays closer to the real axis. (Note that the $\alpha = 0.1$ and $\tau = 0.563$ data do not allow for immediate comparison; they are rather indicative of typical behavior for the respective contours.) The saturation of entanglement observed for all complex contours explains the large accessible times.

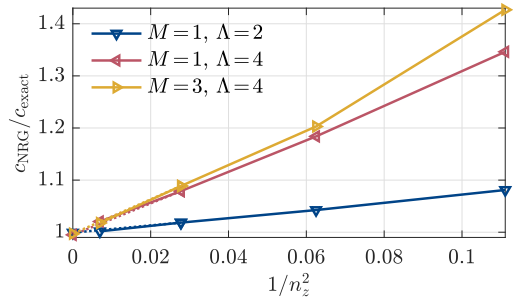


FIG. 14. Coefficient c of $-\text{Im}\Sigma(\omega) = c\omega^2$ obtained in NRG calculations at weak interaction for various M , Λ , and $n_z \in \{3, 4, 6, 12\}$. For each M and Λ , one observes a roughly linear dependence of c_{NRG} in $1/n_z^2$, permitting an extrapolation toward the ideal $n_z = \infty$ limit. The extrapolated value is in perfect agreement with the analytically known result c_{exact} .

Appendix F: NRG extrapolation in n_z

For the cases studied in this paper, the self-energy obeys the zero-temperature Fermi-liquid behavior $-\text{Im}\Sigma(\omega) = c\omega^2$ at low frequencies ω . The NRG result for c is sensitive to the discretization of the hybridization function, i.e., it varies notably with the discretization parameter Λ [47] and the number of z -shifts n_z [57]. The hypothetical continuum limit $\Lambda \rightarrow 1$ is numerically not feasible. For one-orbital calculations, Λ can be chosen as small as, say, 1.7; three-orbital calculations require $\Lambda \gtrsim 4$. The limit of $n_z \rightarrow \infty$ similarly is not feasible. For our one-orbital calculations, we consider n_z values up to 12; for our three-orbital calculations, $n_z \leq 6$.

For the particle-hole symmetric Anderson model with a flat hybridization, $-\text{Im}\Delta(\omega) = \Delta\Theta(D - |\omega|)$, in the wide-band limit ($D \rightarrow \infty$) and at weak interaction $u \equiv U/(\pi\Delta) \ll 1$, the coefficient c is known from second-order perturbation theory [76]. This applies to the one-orbital case [77] and can be readily generalized to multiple orbitals [78] (setting $J = 0$ for simplicity). The result, with M the number of orbitals, is

$$c_{\text{exact}} = \frac{1}{2}u^2M. \quad (\text{F1})$$

We computed NRG results using $D = 100$, $\Delta = 1$, $U = 0.2$, $T = 0$. The coefficient c is deduced from a fit in the frequency range $5 \cdot 10^{-4} < \omega < 5 \cdot 10^{-2}$, after adaptive broadening [60] with $\alpha_z = \alpha/n_z$ and $\alpha = 1$. Figure 14 shows c_{NRG} , for one- and three-orbital calculations and selected values of Λ , for various values of n_z . One observes a roughly linear behavior in $1/n_z^2$, nicely extrapolating to the analytic value c_{exact} at $n_z = \infty$. Not surprisingly, the dependence of c_{NRG} on n_z is stronger for larger Λ . We determined the extrapolated values from the two data points at $n_z = 4$ and $n_z = 6$. The same choice is used for the frequency-dependent self-energies extrapolated in n_z shown in the main text.

Table I summarizes the symmetries used in NRG (**charge**, **spin**, and **orbital** symmetries) and the number

#orbitals M	H_{int}	Symmetry	N_{kp}	N_{kp}^*
1	-	$\text{SU}(2)_{\text{ch}} \otimes \text{SU}(2)_{\text{sp}}$	32k	300k
3	DN	$\text{U}(1)_{\text{ch}} \otimes \text{SU}(2)_{\text{sp}} \otimes \text{SU}(3)_{\text{orb}}$	20k	800k
3	HK	$\text{U}(1)_{\text{ch}} \otimes \text{SU}(2)_{\text{sp}} \otimes \text{SO}(3)_{\text{orb}}$	15k	200k

TABLE I. Symmetries used and number of multiples N_{kp} (or approximate number of states N_{kp}^*) kept during the NRG iterative diagonalization (1k denotes 10^3).

of states kept during the iterative diagonalization. In the three-orbital case, one can distinguish the Hubbard–Kanamori (HK) and the Dworin–Narath (DN) Hamiltonians [63], with $\text{SO}(3)$ and $\text{SU}(3)$ orbital symmetry, respectively. The large $\text{SU}(3)$ orbital symmetry of the DN Hamiltonian (also used here at $J = 0$) allows us to effectively keep a much larger number of states N_{kp}^* than in the calculations of the HK Hamiltonian, so that the former results can be considered significantly more accurate than the latter.

-
- [1] S. R. White, Density matrix formulation for quantum renormalization groups, *Phys. Rev. Lett.* **69**, 2863 (1992).
- [2] S. R. White, Density-matrix algorithms for quantum renormalization groups, *Phys. Rev. B* **48**, 10345 (1993).
- [3] U. Schollwöck, The density-matrix renormalization group in the age of matrix product states, *Annals of Physics* **326**, 96 (2011), january 2011 Special Issue.
- [4] J. Haegeman, C. Lubich, I. Oseledets, B. Vandereycken, and F. Verstraete, Unifying time evolution and optimization with matrix product states, *Phys. Rev. B* **94**, 165116 (2016).
- [5] V. M. F. Verstraete and J. Cirac, Matrix product states, projected entangled pair states, and variational renormalization group methods for quantum spin systems, *Advances in Physics* **57**, 143 (2008), <https://doi.org/10.1080/14789940801912366>.
- [6] S. Paeckel, T. Köhler, A. Swoboda, S. R. Manmana, U. Schollwöck, and C. Hubig, Time-evolution methods for matrix-product states, *Annals of Physics* **411**, 167998 (2019).
- [7] K. A. Hallberg, Density matrix algorithm for the calculation of dynamical properties of low dimensional systems, *Phys. Rev. B* **52**, 9827 (1995).
- [8] T. D. Kühner and S. R. White, Dynamical correlation functions using the density-matrix renormalization group, *Phys. Rev. B* **60**, 335 (1999).
- [9] E. Jeckelmann, Dynamical density-matrix renormalization-group method, *Phys. Rev. B* **66**, 045114 (2002).
- [10] A. Weichselbaum, F. Verstraete, U. Schollwöck, J. I. Cirac, and J. von Delft, Variational matrix-product-state approach to quantum impurity models, *Phys. Rev. B* **80**, 165117 (2009).
- [11] A. Holzner, A. Weichselbaum, I. P. McCulloch, U. Schollwöck, and J. von Delft, Chebyshev matrix product state approach for spectral functions, *Phys. Rev. B* **83**, 195115 (2011).
- [12] P. E. Dargel, A. Wöllert, A. Honecker, I. P. McCulloch, U. Schollwöck, and T. Pruschke, Lanczos algorithm with matrix product states for dynamical correlation functions, *Phys. Rev. B* **85**, 205119 (2012).
- [13] F. A. Wolf, J. A. Justiniano, I. P. McCulloch, and U. Schollwöck, Spectral functions and time evolution from the Chebyshev recursion, *Phys. Rev. B* **91**, 115144 (2015).
- [14] A. Nocera and G. Alvarez, Spectral functions with the density matrix renormalization group: Krylov-space approach for correction vectors, *Phys. Rev. E* **94**, 053308 (2016).
- [15] A. Baiardi, A. K. Kelemen, and M. Reiher, Excited-state DMRG made simple with FEAST, *Journal of Chemical Theory and Computation* **18**, 415 (2022), pMID: 34914392, <https://doi.org/10.1021/acs.jctc.1c00984>.
- [16] G. Vidal, Efficient classical simulation of slightly entangled quantum computations, *Phys. Rev. Lett.* **91**, 147902 (2003).
- [17] G. Vidal, Efficient simulation of one-dimensional quantum many-body systems, *Phys. Rev. Lett.* **93**, 040502 (2004).
- [18] A. J. Daley, C. Kollath, U. Schollwöck, and G. Vidal, Time-dependent density-matrix renormalization-group using adaptive effective Hilbert spaces, *J. Stat. Mech.: Theor. Exp.* (2004), P04005 (2004).
- [19] S. R. White and A. E. Feiguin, Real time evolution using the density matrix renormalization group, *Phys. Rev. Lett.* **93**, 076401 (2004).
- [20] F. Verstraete, J. J. Garcia-Ripoll, and J. I. Cirac, Matrix product density operators: simulation of finite- T and dissipative systems, *Phys. Rev. Lett.* **93**, 207204 (2004).
- [21] M. Zwolak and G. Vidal, Mixed-state dynamics in one-dimensional quantum lattice systems: A time-dependent superoperator renormalization algorithm, *Phys. Rev. Lett.* **93**, 207205 (2004).
- [22] J. Haegeman, J. I. Cirac, T. J. Osborne, I. Pižorn, H. Verschelde, and F. Verstraete, Time-dependent variational principle for quantum lattices, *Phys. Rev. Lett.* **107**, 070601 (2011).
- [23] M. P. Zaletel, R. S. K. Mong, C. Karrasch, J. E. Moore, and F. Pollmann, Time-evolving a matrix product state with long-ranged interactions, *Phys. Rev. B* **91**, 165112 (2015).
- [24] P. Calabrese and J. Cardy, Entanglement entropy and quantum field theory, *Journal of Statistical Mechanics: Theory and Experiment* **2004**, P06002 (2004).
- [25] P. Calabrese and J. Cardy, Evolution of entanglement entropy in one-dimensional systems, *Journal of Statistical Mechanics: Theory and Experiment* **2005**, P04010 (2005).
- [26] J. Eisert and T. J. Osborne, General entanglement scaling laws from time evolution, *Phys. Rev. Lett.* **97**, 150404 (2006).
- [27] S. Bravyi, Upper bounds on entangling rates of bipartite hamiltonians, *Phys. Rev. A* **76**, 052319 (2007).
- [28] T. J. Osborne, Efficient approximation of the dynamics of one-dimensional quantum spin systems, *Phys. Rev. Lett.* **97**, 157202 (2006).

- [29] A. M. Alhambra and J. I. Cirac, Locally accurate tensor networks for thermal states and time evolution, *PRX Quantum* **2**, 040331 (2021).
- [30] N. Schuch, M. M. Wolf, F. Verstraete, and J. I. Cirac, Entropy scaling and simulability by matrix product states, *Phys. Rev. Lett.* **100**, 030504 (2008).
- [31] P. Calabrese and J. Cardy, Entanglement and correlation functions following a local quench: a conformal field theory approach, *Journal of Statistical Mechanics: Theory and Experiment* **2007**, P10004 (2007).
- [32] A. Georges and G. Kotliar, Hubbard model in infinite dimensions, *Phys. Rev. B* **45**, 6479 (1992).
- [33] A. Georges, G. Kotliar, W. Krauth, and M. J. Rozenberg, Dynamical mean-field theory of strongly correlated fermion systems and the limit of infinite dimensions, *Rev. Mod. Phys.* **68**, 13 (1996).
- [34] G. Kotliar, S. Savrasov, K. Haule, V. Oudovenko, O. Parcollet, and C. Marianetti, Electronic structure calculations with dynamical mean-field theory, *Rev. Mod. Phys.* **78**, 865 (2006).
- [35] F. A. Wolf, A. Go, I. P. McCulloch, A. J. Millis, and U. Schollwöck, Imaginary-time matrix product state impurity solver for dynamical mean-field theory, *Phys. Rev. X* **5**, 041032 (2015).
- [36] N.-O. Linden, M. Zingl, C. Hubig, O. Parcollet, and U. Schollwöck, Imaginary-time matrix product state impurity solver in a real material calculation: Spin-orbit coupling in Sr_2RuO_4 , *Phys. Rev. B* **101**, 041101 (2020).
- [37] M. Bramberger, J. Mravlje, M. Grundner, U. Schollwöck, and M. Zingl, BaOsO_3 : A Hund's metal in the presence of strong spin-orbit coupling, *Phys. Rev. B* **103**, 165133 (2021).
- [38] M. Bramberger, B. Bacq-Labreuil, M. Grundner, S. Biermann, U. Schollwöck, S. Paeckel, and B. Lenz, Formation of CuO_2 sublattices by suppression of interlattice correlations in tetragonal CuO , *SciPost Phys.* **14**, 010 (2023).
- [39] M. Ganahl, P. Thunström, F. Verstraete, K. Held, and H. G. Evertz, Chebyshev expansion for impurity models using matrix product states, *Phys. Rev. B* **90**, 045144 (2014).
- [40] F. A. Wolf, I. P. McCulloch, O. Parcollet, and U. Schollwöck, Chebyshev matrix-product state impurity solver for dynamical mean-field theory, *Phys. Rev. B* **90**, 115124 (2014).
- [41] M. Ganahl, M. Aichhorn, H. G. Evertz, P. Thunström, K. Held, and F. Verstraete, Efficient DMFT impurity solver using real-time dynamics with matrix product states, *Phys. Rev. B* **92**, 155132 (2015).
- [42] D. Bauernfeind, M. Zingl, R. Triebl, M. Aichhorn, and H. G. Evertz, Fork tensor-product states: Efficient multi-orbital real-time DMFT solver, *Phys. Rev. X* **7**, 031013 (2017).
- [43] K. Guther, W. Dobrautz, O. Gunnarsson, and A. Alavi, Time propagation and spectroscopy of fermionic systems using a stochastic technique, *Phys. Rev. Lett.* **121**, 056401 (2018).
- [44] X. Cao, Y. Lu, E. M. Stoudenmire, and O. Parcollet, Dynamical correlation functions from complex time evolution (2023), [arXiv:2311.10909 \[cond-mat.str-el\]](https://arxiv.org/abs/2311.10909).
- [45] K. G. Wilson, The renormalization group: Critical phenomena and the Kondo problem, *Rev. Mod. Phys.* **47**, 773 (1975).
- [46] H. R. Krishna-murthy, J. W. Wilkins, and K. G. Wilson, Renormalization-group approach to the Anderson model of dilute magnetic alloys. I. Static properties for the symmetric case, *Phys. Rev. B* **21**, 1003 (1980).
- [47] R. Bulla, T. A. Costi, and T. Pruschke, Numerical renormalization group method for quantum impurity systems, *Rev. Mod. Phys.* **80**, 395 (2008).
- [48] P. W. Anderson, Localized magnetic states in metals, *Phys. Rev.* **124**, 41 (1961).
- [49] C. Raas and G. S. Uhrig, Spectral densities from dynamic density-matrix renormalization, *The European Physical Journal B - Condensed Matter and Complex Systems* **45**, 293 (2005).
- [50] J. R. Schrieffer and P. A. Wolff, Relation between the Anderson and Kondo Hamiltonians, *Phys. Rev.* **149**, 491 (1966).
- [51] I. de Vega, U. Schollwöck, and F. A. Wolf, How to discretize a quantum bath for real-time evolution, *Phys. Rev. B* **92**, 155126 (2015).
- [52] C. Karrasch, J. H. Bardarson, and J. E. Moore, Reducing the numerical effort of finite-temperature density matrix renormalization group calculations, *New Journal of Physics* **15**, 083031 (2013).
- [53] T. Barthel, Precise evaluation of thermal response functions by optimized density matrix renormalization group schemes, *New Journal of Physics* **15**, 073010 (2013).
- [54] C. Hubig, F. Lachenmaier, N.-O. Linden, T. Reinhard, L. Stenzel, A. Swoboda, M. Grundner, and S. Mardazad, *The SYTEN toolkit*.
- [55] A. Weichselbaum and J. von Delft, Sum-rule conserving spectral functions from the numerical renormalization group, *Phys. Rev. Lett.* **99**, 076402 (2007).
- [56] R. Peters, T. Pruschke, and F. B. Anders, Numerical renormalization group approach to green's functions for quantum impurity models, *Phys. Rev. B* **74**, 245114 (2006).
- [57] R. Žitko and T. Pruschke, Energy resolution and discretization artifacts in the numerical renormalization group, *Phys. Rev. B* **79**, 085106 (2009).
- [58] A. Weichselbaum, Tensor networks and the numerical renormalization group, *Phys. Rev. B* **86**, 245124 (2012).
- [59] S.-S. B. Lee, J. von Delft, and A. Weichselbaum, Doublon-holon origin of the subpeaks at the hubbard band edges, *Phys. Rev. Lett.* **119**, 236402 (2017).
- [60] S.-S. B. Lee and A. Weichselbaum, Adaptive broadening to improve spectral resolution in the numerical renormalization group, *Phys. Rev. B* **94**, 235127 (2016).
- [61] A. Weichselbaum, Non-abelian symmetries in tensor networks: A quantum symmetry space approach, *Annals of Physics* **327**, 2972 (2012).
- [62] F. B. Kugler, Improved estimator for numerical renormalization group calculations of the self-energy, *Phys. Rev. B* **105**, 245132 (2022).
- [63] A. Georges, L. de Medici, and J. Mravlje, Strong correlations from Hund's coupling, *Annual Review of Condensed Matter Physics* **4**, 137 (2013).
- [64] K. Gunst, F. Verstraete, S. Wouters, O. Legeza, and D. Van Neck, T3NS: Three-legged tree tensor network states, *J. Chem. Theory Comput.* **2018**, *14*, 4, 2026–2033 **14**, 2026 (2018).
- [65] D. Bauernfeind and M. Aichhorn, Time dependent variational principle for tree Tensor Networks, *SciPost Phys.* **8**, 024 (2020).
- [66] K. M. Stadler, Z. P. Yin, J. von Delft, G. Kotliar, and A. Weichselbaum, Dynamical mean-field theory plus numerical renormalization-group study of spin-orbital sepa-

- ration in a three-band Hund metal, *Phys. Rev. Lett.* **115**, 136401 (2015).
- [67] A. Horvat, R. Žitko, and J. Mravlje, Low-energy physics of three-orbital impurity model with kanamori interaction, *Phys. Rev. B* **94**, 165140 (2016).
- [68] A. Horvat, R. Žitko, and J. Mravlje, Spin-orbit coupling in three-orbital kanamori impurity model and its relevance for transition-metal oxides, *Phys. Rev. B* **96**, 085122 (2017).
- [69] F. B. Kugler, S.-S. B. Lee, A. Weichselbaum, G. Kotliar, and J. von Delft, Orbital differentiation in hund metals, *Phys. Rev. B* **100**, 115159 (2019).
- [70] A. K. Mitchell, M. R. Galpin, S. Wilson-Fletcher, D. E. Logan, and R. Bulla, Generalized wilson chain for solving multichannel quantum impurity problems, *Phys. Rev. B* **89**, 121105 (2014).
- [71] K. M. Stadler, A. K. Mitchell, J. von Delft, and A. Weichselbaum, Interleaved numerical renormalization group as an efficient multiband impurity solver, *Phys. Rev. B* **93**, 235101 (2016).
- [72] F. B. Kugler, M. Zingl, H. U. R. Strand, S.-S. B. Lee, J. von Delft, and A. Georges, Strongly correlated materials from a Numerical Renormalization Group perspective: How the Fermi-liquid state of sr_2ruo_4 emerges, *Phys. Rev. Lett.* **124**, 016401 (2020).
- [73] F. B. Kugler and G. Kotliar, Is the orbital-selective mott phase stable against interorbital hopping?, *Phys. Rev. Lett.* **129**, 096403 (2022).
- [74] M. Jarrell and J. E. Gubernatis, Bayesian inference and the analytic continuation of imaginary-time quantum Monte Carlo data, *Physics Reports* **269**, 133 (1996).
- [75] J. Skilling, Classic maximum entropy, in *Maximum Entropy and Bayesian Methods: Cambridge, England, 1988* (Springer, 1989) pp. 45–52.
- [76] V. Zlatić and B. Horvatić, Series expansion for the symmetric anderson hamiltonian, *Phys. Rev. B* **28**, 6904 (1983).
- [77] K. Yamada, Perturbation Expansion for the Anderson Hamiltonian. II, *Prog. Theor. Phys.* **53**, 970 (1975).
- [78] Y. Nishikawa, D. J. G. Crow, and A. C. Hewson, Renormalized parameters and perturbation theory for an n -channel anderson model with hund's rule coupling: Symmetric case, *Phys. Rev. B* **82**, 115123 (2010).